Published in final edited form as:
Magn Reson Med. 2014 June ; 71(6): 2197–2205. doi:10.1002/mrm.24863.

Susceptibility Weighted Imaging of Cartilage Canals in Porcine Epiphyseal Growth Cartilage Ex Vivo and In Vivo

Mikko J. Nissi[1,2,*], **Ferenc Toth**[3], **Jinjin Zhang**[1,2,4], **Sebastian Schmitter**[1], **Michael Benson**[1,2], **Cathy S. Carlson**[3], and **Jutta M. Ellermann**[1]

[1]Center for Magnetic Resonance Research and Department of Radiology, University of Minnesota, Minneapolis, Minnesota, USA

[2]Department of Orthopaedic Surgery, University of Minnesota, Minneapolis, Minnesota, USA

[3]Department of Veterinary Population Medicine, College of Veterinary Medicine, University of Minnesota, St. Paul, Minnesota, USA

[4]School of Physics and Astronomy, University of Minnesota, Minneapolis, Minnesota, USA

Abstract

Purpose—High-resolution visualization of cartilage canals has been restricted to histological methods and contrast-enhanced imaging. In this study, the feasibility of non-contrast-enhanced susceptibility weighted imaging (SWI) for visualization of the cartilage canals was investigated ex vivo at 9.4 T, further explored at 7 and 3 T and demonstrated in vivo at 7 T, using a porcine animal model.

Methods—SWI scans of specimens of distal femur and humerus from 1 to 8 week-old piglets were conducted at 9.4 T using 3D-GRE sequence and SWI post-processing. The stifle joints of a 2-week old piglet were scanned ex vivo at 7 and 3 T. Finally, the same sites of a 3-week-old piglet were scanned, in vivo, at 7 T under general anesthesia using the vendor-provided sequences.

Results—High-contrast visualization of the cartilage canals was obtained ex vivo, especially at higher field strengths; the results were confirmed histologically. In vivo feasibility was demonstrated at 7 T and comparison of ex vivo scans at 3 and 7 T indicated feasibility of using SWI at 3 T.

Conclusions—High-resolution 3D visualization of cartilage canals was demonstrated using SWI. This demonstration of fully noninvasive visualization opens new avenues to explore skeletal maturation and the role of vascular supply for diseases such as osteochondrosis.

Keywords

susceptibility weighted imaging; cartilage canals; imaging; epiphyseal cartilage

[*]Correspondence to: Mikko J. Nissi, Ph.D., CMRR and Departments of Radiology and Orthopaedic Surgery, University of Minnesota, 2021 6th Street SE, Minneapolis, MN 55455. nissi@cmrr.umn.edu.

Additional Supporting Information may be found in the online version of this article.

Susceptibility weighted imaging (SWI) is a recent technique, used primarily for neuroimaging that uses subtle differences in magnetic susceptibility values between different tissues to generate contrast (1-3). As opposed to standard, magnitude-only, proton density, T_1 or T_2 weighted imaging. SWI also incorporates the use of phase data in contrast generation (4). The phase data contain information on local susceptibility changes between tissues (high spatial frequency phase changes) as well as on static inhomogeneous background magnetic fields (low spatial frequency phase changes). The latter phase components may mask the tissue-related phase information (1,4,5), however, by applying an appropriate high pass filter (4) or using alternative methods for "phase unwrapping" (6,7), the unwanted low frequency component may be filtered out.

Phase contrast and SWI are used mainly in imaging of brain vasculature (1,2), iron content (8), direct visualization of brain anatomy (3,5,9), hemorrhages and brain lesions (10,11), and quantification of oxygen saturation (12). The difference of ~0.2 ppm (13,14) in magnetic susceptibility between deoxygenated blood and surrounding tissue leads to the accumulation of a phase difference between the venous blood and surrounding tissues (1). The resulting contrast due to phase accumulation is more easily depicted at higher field strengths since the amplitude of susceptibility induced local field variations is linearly proportional to the main magnetic field (4). Alternatively, the higher signal to noise ratios (SNR) available at higher field strengths can be used to shorten data acquisition time or to achieve higher spatial resolution while maintaining phase contrast at a same level (4). Additionally, the source of the SWI contrast can be of subvoxel size and still contribute to detectable signal differences (4).

The vasculature of the developing skeleton particularly that of epiphyseal growth cartilage has a critical role in supplying nutrients. The vasculature in epiphyseal growth cartilage is confined to "cartilage canals," channels that contain both arterioles and venules. Larger canals have been reported to range from 0.2 to 0.6 mm (average 0.3 mm) in piglets of 1–4 weeks of age with the vessels in the canals ranging from 0.01 to 0.16 mm in diameter (15). In animal models, it has been shown that a disruption of the cartilage canal blood supply causes tissue necrosis, which in turn may hinder ossification leading to the development of osteochondrosis (16,17). While this pathogenesis has been reported in animal models using histological evaluations, similar investigations have not been reported in humans due, in large part, to lack of noninvasive investigational tools. Only a few publications have described imaging of cartilage canals using MRI. Babyn et al. reported visualization of porcine cartilage canals in 3 mm biopsy cores with T2-weighted high-resolution MR imaging (18). Jaramillo et al. (19) later demonstrated the use of Gadolinium enhanced imaging of the cartilage canals in piglets, followed shortly by Barnewolt et al. (20), demonstrating distinct age dependent patterns of vascular canal orientation and distribution in human infants. Other reports have also demonstrated the use of Gadolinium-enhanced visualization of cartilage canals (15,21).

The science of visualizing cartilage canals, however, is still in its infancy. Imaging of cartilage canals using intravenous Gadolinium contrast agent is limited by the short useful scanning time window and the SNR and resolution achievable; specifically, visualization of the network of smaller vessels using Gadolinium appears very limited (15,20). Furthermore,

especially when imaging children, tissue inherent contrast is preferred over the administration of exogeneous contrast agents. To date, the intricate system of cartilage canals has only been visualized using ex vivo animal systems. The only anatomical studies demonstrating high-resolution images of the cartilage canals have used gold standard histological methods or intravenous contrast injection followed by tissue clearing and photography (16,22). An imaging method for utilizing inherent tissue contrast for high-resolution imaging of cartilage canals without the administration of intravenous contrast agent is highly desirable and would allow in vivo assessment of cartilage canal blood supply in normal and diseased epiphyseal cartilage.

The purpose of this study was to investigate the feasibility of using SWI contrast to visualize cartilage canals in a porcine model, both ex vivo and in vivo. The first hypothesis of the study was that SWI would enable imaging and three dimensional (3D) visualization of the cartilage canals in postmortem specimens of epiphyseal growth cartilage. To test the hypothesis, specimens of porcine distal femur and distal humerus were imaged ex vivo using SWI at 9.4 T. After high-field ex vivo investigation, the second hypothesis was that SWI is also feasible for imaging the cartilage canals in vivo. To test this hypothesis and explore the in vivo feasibility, a live piglet was imaged at 7.0 T. Since 7.0 T is not yet clinically approved, an additional ex vivo experiment was conducted at 3.0 T to estimate the feasibility of using this technique at a clinically available magnetic field strength.

METHODS

Specimens

All animal procedures were approved by the institutional animal care and use committee of the University of Minnesota (protocol: 1111A06521). For the ex vivo part of the study, piglets of ages 1–6 weeks were obtained from a commercial provider. From each animal, the right distal femur and humerus were harvested for MR imaging and the left limbs were perfused with radio-opaque contrast medium (Barium sulfate, Sol-O-Pake, E-Z-EM, Westbury, NY 11590-5021) for μCT scanning. The harvested specimens were stored frozen at −80°C wrapped in saline soaked paper towels and sealed in plastic bags until they were thawed at room temperature for MRI studies. For initial testing, samples from the distal femur of a piglet of ~8 weeks of age that was presented for necropsy were harvested.

For the in vivo part of the study, a 3-week-old piglet was premedicated using Telazole administered intramuscularly, after which anesthesia was maintained by inhalation of isoflurane vaporized in oxygen. At the conclusion of the procedure, the pig was euthanized using intravenously administered KCL.

To compare in vivo and ex vivo results, the carcass of a 2-week-old piglet was imaged at 7.0 T and frozen at −20°C. To explore further the feasibility of the method at a clinically relevant 3.0 T field strength, the same carcass was subsequently thawed at room temperature for ~22 h and imaged at 3.0 T.

MR Imaging

Ex vivo imaging was conducted on a 9.4 T Agilent scanner driven with the VnmrJ software version 3.1. A quadrature volume transceiver coil (Millipede, Varian NMR Systems, Palo Alto, CA) was used for all acquisitions. The specimens were placed in test tubes immersed in perfluoropolyether for clean background on MR images and to avoid susceptibility mismatch on tissue-air interfaces. To properly fit the samples and load the coil, the distal femoral specimens were generally oriented with femoral shafts along B0. The distal humeral specimens were oriented with the axis of the humeral trochlea along the B0. Initial parameter exploration was done using two-dimensional (2D) gradient recalled echo sequence with TR = 50 ms, receiver bandwidth = 100 kHz, 1 mm slice, and 100 μm in-plane resolution using varying echo times (TEs). SWI datasets were acquired using a 3D gradient recalled echo sequence with an isotropic resolution of ~100 μm, adjusting the FOV and matrix size to fit the specimens; the FOV sizes were generally 40 mm^3 or less depending on the individual specimen sizes (scan times with one average varied from 43 to 98 min depending on the number of voxels acquired; Table 1).

In vivo imaging of the stifle joints was conducted at 7.0 T (Magnetom 7 T, Siemens, Erlangen, Germany) using an 8-channel transmit/receive knee coil (Virtumed, LLC Minneapolis, MN) driven by a B1 shimming unit (CPC, Hauppauge, NY) with 8 × 1 kW amplifiers. Transmit B1 (B1+) shimming (23) was applied within a manually defined region of interest to maximize flip angle homogeneity (24). B1+ maps were calibrated with a fast estimation technique as previously described (23,25,26) and subsequently, a set of B1+ phases for the 8 channels was calculated in Matlab (The Mathworks, Natick, MA) to minimize the coefficient of variation of the resulting |B1+| (23).

SWI scans were acquired using 3D GRE sequence with manufacturer provided SWI-option enabled (i.e., switching on the standard SWI acquisition and post-processing options as determined by the vendor-provided protocol). Further parameter adjustments were as follows: FOV was set as small as possible while avoiding folding; the acquisition parameters are listed in Table 1.

Ex vivo imaging at 7.0 T used a protocol nearly identical with the in vivo scan with minimal differences in scanning parameters and in the applied B1+ shimming solution (Table 1). The ex vivo scanning was subsequently repeated at 3.0 T (MAGNETOM Tim Trio™, Siemens Erlangen, Germany). At 3.0 T the FOV was also chosen to be as small as possible. A single channel knee coil without accelerations was used for acquisition (Table 1).

Image Processing

The SWI-post-processing of the 9.4 T ex vivo 3D GRE data was done according to earlier reports (4,27). Briefly, the process consists of (1) unwrapping the phase data, (2) creating a phase mask, and (3) applying the phase mask to magnitude data. The phase unwrapping was done by complex dividing the original image with one reconstructed from the central portion of the k-space (i.e., high-pass filtering) (4). Haacke et al. (4) suggested using 1/8 of the width of the k-space for constructing high pass filtering image. In this work, however, 1/6 and 1/4 of the width of the (3D) k-space was used for filter construction after initial testing

on optimal filter sizes (14,27,28). The created high-frequency phase data was then converted to a negative phase mask [i.e., mask = 0 … 1 for phase = −π … 0 and mask = 1 for phase > 0 (4)], which was subsequently multiplied to the original magnitude data. Different numbers of phase mask multiplications were tested and visually evaluated and, finally, 6 multiplications was applied. For the ex vivo scans at 3.0 and 7.0 T, SWI post-processing provided by the scanner manufacturer was used. For the in vivo scan at 7.0 T, both vendor-provided and in-house post-processing were done (for comparison, see Supporting Information).

For visualization purposes, minimum intensity projections (mIPs) of varying thickness were created from the SWI data. For ex vivo specimens, different masking and thresholding schemes together with morphological processing of the masks were applied for clearing up signal from background and bone. Reslicing of the SWI data in arbitrary planes as well as 3D volume rendering of masked and contrast-inverted SWI datasets were created using Osirix (Osirix v.5.0.2 32-bit, http://www.osirix-viewer.com/; (29)).

Reference Methods

After MR imaging, all samples were decalcified in 10% EDTA and processed for histological examination. Toluidine blue and Hematoxylin and eosin –stained histological sections were prepared in a standard fashion and scanned at high resolution (2400 dpi) using a flatbed film scanner (Epson Perfection V750 Pro, Seiko Epson Corp, Japan). The contralateral barium-perfused specimens underwent μCT imaging using a Siemens Inveon preclinical μPET/CT scanner (Siemens Medical Solutions, USA). The tube voltage and current were 80 kV and 500 μA, respectively and a voxel resolution of 47.7 μm was obtained. Maximum intensity projections of 2 mm thickness were created from regions approximately corresponding to the SWI data of the contralateral limb.

RESULTS

Different filter sizes indicated visually optimal contrast between the cartilage canals and surrounding tissue while avoiding significant artifacts by using the central 1/6–1/4 of the k-space width for phase unwrapping ex vivo at 9.4 T (Fig. 1). Furthermore, the number of subsequent phase mask multiplications into the original magnitude images suggested that the best contrast was achieved with 4–6 multiplications of the phase mask (Fig. 1).

The effect of the TE on the contrast between the cartilage canals and the surrounding epiphyseal growth cartilage was investigated ex vivo at 9.4 T using a 2D GRE sequence with varying TE. Both the unprocessed GRE magnitude images and the filtered phase images revealed the vessels at short TEs (~8–12 ms), and the contrast increased with increasing TE (Fig. 2). However, at longer TEs, the artifacts also became increasingly prominent.

The raw 3D GRE data faintly depicted the cartilage canals, but visualization was substantially improved after the post-processing at 9.4 T (Fig. 3). mIP over a thickness of 2 mm (~20 consecutive imaging slices for the 9.4 T ex vivo specimens) revealed the course of the cartilage canals, as exemplified in the distal femur (Fig. 3). For the mIPs, the (dark)

image background and (dark) bone were first segmented out using the unprocessed data to avoid signal voids in the mIP tracing.

Matching spatial distribution of the cartilage canals, as confirmed by gold standard histology in a 2D plane was revealed by reslicing the 3D 9.4 T SWI data in the plane of the histological sections. A clear spatial correspondence between the SWI-detected cartilage canals and actual cartilage canals (histology) was confirmed (Fig. 4). To establish a coarse size detection limit of ex vivo SWI at 9.4 T with ~100 μm isotropic resolution, diameters of 50 of the cartilage canals (focusing on the smallest ones) that were detected by SWI were measured from the histology sections. The average diameter of these canals was 104 ± 23 μm, with a range from 55 to 154 μm. For the in vivo SWI at 7.0 T, the respective average diameter of the smallest detected canals was 200 ± 46 μm, with a range from 134 to 301 μm (n = 30). The μCT scans of the perfused contralateral specimens demonstrated visual similarity in the vessel patterns (Fig. 4).

3D visualization of the 9.4 T SWI dataset after contrast inversion and appropriate color lookup table creation revealed the distribution and orientation of the cartilage canals within the entire epiphyseal growth cartilage in distal femoral as well as distal humeral specimen (Fig. 5).

Feasibility of the SWI method in vivo was demonstrated at 7.0 T (Fig. 6). Comparison of the in vivo and ex vivo SWI datasets from the live piglet or the carcass imaged at 7.0 T demonstrated that the signal induced by the inherent susceptibility differences between cartilage canals and surrounding tissue could be visualized not only ex vivo, but also in vivo (Fig. 6). Minuscule differences in the imaging parameters (especially receiver bandwidth and number of averages) contributed to the SNR differences seen. The same carcass, scanned at 3.0 T, demonstrated visualization of the cartilage canals at clinically feasible field strength (Fig. 6). Decrease in SNR and achievable resolution was also noted with the scanning setup used (single channel coil) at 3.0 T. Vendor-provided post-processing and in-house post-processing using ~1/3 of the central k-space for phase unwrapping and 4 multiplications of a positive phase mask for the in vivo 7.0 T data provided results that were visually nearly indistinguishable.

Clear dipolar pattern in the phase signal around cartilage canals was noted, especially in the high-resolution images obtained ex vivo at 9.4 T (Fig. 7). Depending on the view orientation with respect to the orientation of the main magnetic field B0, either a spot of negative phase surrounded by a [faint] halo of positive phase (Fig. 7a), or two separated spots of negative phase with a positive phase in between (Fig. 7b,c) were observed. For vessels running perpendicular to the B0, this dipolar phase resulted in a “doubling” artifact, whereas for vessels running parallel to B0, the doubling was masked (Fig. 7b,c). In the axial plane (plane perpendicular to the B0), no “doubling” could be detected, especially in minimum intensity projected data.

DISCUSSION

This work demonstrated the use of SWI for high resolution imaging of the cartilage canals in epiphyseal growth cartilage. Moreover, the in vivo feasibility of the method was demonstrated at 7.0 T and explored further at clinically applicable field strength of 3.0 T by comparing ex vivo data obtained from the same carcass at both field strengths. The utilization of tissue inherent contrast with SWI for cartilage canal visualization appeared to yield substantial improvement over previously demonstrated contrast-enhanced imaging with intravenous Gadolinium (15,20,21).

High resolution SWI imaging of ex vivo specimens at 9.4 T demonstrated that the vascular structures became visible at fairly short TEs of ~8–12 ms, without any processing of the data. Contrast between the vessels and cartilage matrix was improved by increasing the TE to 14–15 ms with minimal sacrifice in image quality or SNR, while longer TEs presented increasingly more unwanted artifacts as well as notable overall signal loss. The TE used was chosen based on the 2D GRE optimization experiment; while this TE provided desired contrast in the 3D acquisition, it may still be suboptimal. The SWI post-processing (4) drastically improved the vessel identification. Instead of the suggested 1/8 of the width of the k-space [64 × 64 central portion of 512 × 512 k-space (4)] for homodyne phase unwrapping, 1/6 in the case of distal femoral specimen and 1/4 in the case of distal humeral specimen appeared to be more appropriate in this study. Restriction of the filtering to lower frequencies (1/8 of the k-space) resulted in more visible artifacts. A good compromise between enhancing visualization of the vessel structures and increasing visible phase artifacts was determined based on visual assessment, as done previously (28). Alternatively, the most appropriate filter size could be determined by finding the minimum size that removes the phase wraps (7), or more advanced phase wrap removal techniques could be used (6). The effect of the multiplication of the phase mask was investigated and 6 multiplications was generally found to provide visually the most informative results.

The vendor-provided post-processing algorithm used on the 7.0 T system (Siemens, software version VB17) was found to be nearly identical to in-house post-processing (a visual comparison between the two implementations can be found in the Supporting Information). The in-house post-processing was repeated for the in vivo 7.0 T data using unfiltered phase images and magnitude images, transforming them to k-space and subsequently using ~1/3 of the width of k-space for homodyne filtering followed by 4 multiplications of a positive phase mask (4). On the 7.0 T scanner, if the “SWI” scan option was selected in the protocol, the generated phase images were preunwrapped (i.e., prefiltered and thus not useful for full off-line post-processing), and unfiltered if the option was not set. Other scanner vendors may have similar options; for unfiltered phase and magnitude data it is possible to repeat the post-processing according to Haacke et al. (4) and determine optimal settings for visualization, or rely on the vendor-provided post-processing if the data has been preprocessed.

The distribution of the cartilage canals, as visualized by SWI, was confirmed histologically. Manual reslicing of the SWI dataset in a slice matching the histological sectioning plane provided an excellent match between the two modalities. For the high-resolution SWI data

acquired at 9.4 T, using a coil just large enough to fit the sample, the correspondence between SWI and histology was very easily demonstrated, with cartilage canals as small as ~100 μm in diameter detected using SWI. Similarly, the μCT maximum intensity projections of matching thickness in the contralateral limb demonstrated visual agreement regarding the appearance of the vessels. For the in vivo and ex vivo SWI data obtained at lower field strengths and with significantly lower resolution (~15–52 times the voxel volume of the 9.4 T ex vivo data), the comparison with histological sections was feasible, but the matching was not ideal due to poorer resolution.

mIPs of varying thicknesses of the SWI data, after thresholding the specimens and background signals, proved qualitatively very informative (see Figs. 3,4, and 7): the topography of the cartilage canals could be appreciated from slightly thicker projections in different parts of the epiphyseal growth cartilage, as well as in the growth plate. Similar vascular patterns as observed by Barnewolt et al. (20) were seen in the femoral specimens. Furthermore, the mIPs clearly demonstrated some of the limitations of the SWI post-processing method currently utilized (see Fig. 7 and discussion below).

In an earlier report, a high resolution T2w image of an ex vivo core (18; Fig. 3 in the reference) demonstrated cartilage canals without the use of a contrast agent. However, enhanced visualization of the canals at approximately similar resolution was achieved using SWI at 9.4 T in this study. Later reports have demonstrated Gadolinium-enhanced imaging of the cartilage canals in juvenile humans, however with markedly less sharp boundaries between the vasculature and surrounding cartilage matrix than was achieved in this study (15,21,30). Both nonionic Gadolinium chelate, gadoteridol (Gd-HPDO3A; 15), or anionic chelate, gadopentetate (Gd-$DTPA^{2-}$; 20), which have been previously used for imaging cartilage canals are not strictly intravascular agents and, therefore, are inherently inadequate for imaging smaller vessels, since the contrast agent rapidly diffuses to the extravascular space (15).

In vivo imaging of the cartilage canals using SWI at 7.0 T was easily accomplished; the location and course of the vessels were clearly depicted in the acquired data. The resolution achieved (0.25 mm isotropic) lacked the detail of 9.4 T ex vivo imaging (with the size detection limit of ~200 μm), but markedly exceeded that of 3.0 T, where an isotropic resolution of 0.375 mm was achieved with the coil used. The size detection limit, semiquantitatively estimated in this study using measurements on histological sections appeared slightly larger then previously predicted for 7.0 T (31). The level of detail appreciated from the in vivo imaging at 7.0 T was very similar to the detail observed ex vivo at 7.0 T. This suggests that the potential decrease in the amount of deoxygenated blood in vivo as compared with ex vivo specimens, and the concomitant decrease in the contrast between vessels and surrounding tissue, did not diminish the potential of the method in vivo.

Due to the shorter RF wavelength at ultra-high magnetic field, the B1+ magnitude typically shows significant spatial variations over the target region, generating nonuniform flip angles and thus nonuniform contrast. For the acquisitions at 9.4 T, only a very small sample (~3–4 cm) was imaged using a single-channel volume coil, without the possibility or even need for B1+ shimming. However, at 7.0 T an 8-channel transceiver coil in combination with a B1+

shimming system was available and uniform contrast was desired for the SWI scans over the target region that included both knees. To improve the spatial homogeneity of |B1+| within this target region, B1+ phase shimming was performed prior to the SWI scan. As a result, for both ex vivo and in vivo scans, optimization of the transmit B1 field improved the uniformity of the contrast.

To explore the feasibility at clinically relevant field strength of 3.0 T, the same ex vivo specimen scanned at 7.0 T was also scanned at 3.0 T. Generally, there is a clear difference in the feasibility of SWI between 3.0 and 7.0 T due to increased SNR and more pronounced susceptibility effect at higher field strength (4,8,31). To achieve the same amount of phase contrast at 3.0 T, the TE must be increased, thus almost necessarily increasing the scan time (4,10,28). Furthermore, as the SNR is also reduced by moving from 7.0 to 3.0 T, the overall feasibility of SWI is decreased (4,9). However, the SWI scan of the ex vivo piglet demonstrated that the vessels can be visualized similarly to 7.0 T. It is worth noting that the carcass imaged at both fields underwent one freeze-thaw cycle between the 7.0 and 3.0 T scans, potentially slightly affecting the results. The SWI image quality at 3.0 T was not significantly better or worse from what has been previously demonstrated using Gadolinium-enhanced imaging, however, the scan provided a 3D dataset throughout the imaged joint(s) at very high isotropic resolution as compared with previous reports acquiring a few slices with slice thicknesses of 1 mm or more (15,20). In this study, the coil used at 3.0 T was a single channel coil and did not permit using parallel acquisition to speed up imaging or for collecting more averages as was done at 7.0 T. The authors are confident that, by using a higher quality multichannel coil with better overall SNR, the visualization of cartilage canals at 3.0 T using SWI could be improved. Altogether, the demonstration of cartilage canal visualization at 3.0 T using the same animal that was scanned at 7.0 T, combined with the fact that no significant differences were observed between ex vivo and in vivo results at 7.0 T, indicated that cartilage canal imaging is feasible using SWI at the clinically available field strength of 3.0 T, using scanning times that are clinically attainable.

The abundance of cartilage canals in piglets, as well as evidence of their importance has been demonstrated earlier in histological studies (16,20). High resolution ex vivo imaging as well as μCT and histological confirmation necessitated the use of an animal model in this study; however, after this initial demonstration of in vivo feasibility, future studies may include the imaging of children with the expectation that new and important findings will be gained.

An interesting finding in the high-resolution ex vivo SWI data was the dipole-field appearing phase pattern around vessels oriented perpendicular to the main field. This dipole-field appearance is a phenomenon that has been reported previously for SWI (7,12,13). This resulted in artifactual “doubling” of the vessels after creating a negative phase mask and applying it to the magnitude data. Less aggressive phase removal (i.e., application of a smaller fraction of k-space for filtering) left larger residual blooming in the phase data, masking some of the doubling and provided improved visualization. More accurate removal of the background phase rather than simple high-pass filtering (6,14), and perhaps more significantly, actual quantitative mapping of the susceptibility (7,12) is likely to improve the

visualization of the vessels in terms of removal of the “doubling” artifact, as well as providing a way to correctly estimate the sizes (diameters) of the vessels from the MRI data.

The method presented in this study for imaging cartilage canals in epiphyseal growth cartilage is likely to lend itself to pediatric in vivo imaging using a 3.0 T clinical scanner, with routinely available and safe non-contrast SWI methods that have low RF deposition. Minimal optimization of the sequence parameters to adapt a brain-imaging protocol for cartilage canals is required; the parameters presented for 3.0 and 7.0 T may serve as starting points for further optimizations. With modern multichannel high quality coils, good visualization results are likely to be achieved.

CONCLUSIONS

In this work, feasibility of imaging cartilage canals in epiphyseal growth cartilage using non-contrast-enhanced SWI was demonstrated. Utilization of the inherent susceptibility contrast between the vessels and the surrounding tissue, without administration of external intravenous contrast agents, not only eliminates the risk associated with contrast media, but also provides a way of acquiring high-resolution 3D data with exquisite specificity for cartilage canals in the developing skeleton. Further research efforts in SWI of cartilage canals are warranted, including improvements in post-processing to resolve the doubling artifact. However, based on this demonstration of high-resolution 3D visualization of cartilage canals with SWI, new avenues to explore skeletal maturation and the role of vascular supply for disease entities in which cartilage canal vessels are damaged will become feasible.

Supplementary Material

Refer to Web version on PubMed Central for supplementary material.

Acknowledgments

The authors are grateful to Drs. Noam Harel and Pierre-Francois Van De Moortele for helpful discussions and comments on the manuscript and to Dr. Bruce Hammer for his help obtaining μCT images.

Grant sponsor: NIH; Grant numbers: T32OD010993, K18OD010468, P41 EB015894, S10 RR26783, and R21 EB009138; Grant sponsor: WM KECK Foundation.

References

1. Reichenbach JR, Venkatesan R, Schillinger DJ, Kido DK, Haacke EM. Small vessels in the human brain: MR venography with deoxyhemoglobin as an intrinsic contrast agent. Radiology. 1997; 204:272–277. [PubMed: 9205259]
2. Haacke EM, Xu Y, Cheng YC, Reichenbach JR. Susceptibility weighted imaging (SWI). Magn Reson Med. 2004; 52:612–618. [PubMed: 15334582]
3. Duyn JH, van Gelderen P, Li TQ, de Zwart JA, Koretsky AP, Fukunaga M. High-field MRI of brain cortical substructure based on signal phase. Proc Natl Acad Sci USA. 2007; 104:11796–11801. [PubMed: 17586684]
4. Haacke EM, Mittal S, Wu Z, Neelavalli J, Cheng YC. Susceptibility-weighted imaging: technical aspects and clinical applications, part 1. AJNR Am J Neuroradiol. 2009; 30:19–30. [PubMed: 19039041]

5. Abduljalil AM, Schmalbrock P, Novak V, Chakeres DW. Enhanced gray and white matter contrast of phase susceptibility-weighted images in ultra-high-field magnetic resonance imaging. J Magn Reson Imaging. 2003; 18:284–290. [PubMed: 12938122]
6. Liu T, Khalidov I, de Rochefort L, Spincemaille P, Liu J, Tsiouris AJ, Wang Y. A novel background field removal method for MRI using projection onto dipole fields (PDF). NMR Biomed. 2011; 24:1129–1136. [PubMed: 21387445]
7. Shmueli K, de Zwart JA, van Gelderen P, Li TQ, Dodd SJ, Duyn JH. Magnetic susceptibility mapping of brain tissue in vivo using MRI phase data. Magn Reson Med. 2009; 62:1510–1522. [PubMed: 19859937]
8. Yao B, Li TQ, Gelderen P, Shmueli K, de Zwart JA, Duyn JH. Susceptibility contrast in high field MRI of human brain as a function of tissue iron content. NeuroImage. 2009; 44:1259–1266. [PubMed: 19027861]
9. Abosch A, Yacoub E, Ugurbil K, Harel N. An assessment of current brain targets for deep brain stimulation surgery with susceptibility-weighted imaging at 7 tesla. Neurosurgery. 2010; 67:1745–1756. discussion 1756. [PubMed: 21107206]
10. Barnes SR, Haacke EM. Susceptibility-weighted imaging: clinical angiographic applications. Magn Reson Imaging Clin N Am. 2009; 17:47–61. [PubMed: 19364599]
11. Wang M, Dai Y, Han Y, Haacke EM, Dai J, Shi D. Susceptibility weighted imaging in detecting hemorrhage in acute cervical spinal cord injury. Magn Reson Imaging. 2011; 29:365–373. [PubMed: 21232894]
12. Haacke EM, Tang J, Neelavalli J, Cheng YC. Susceptibility mapping as a means to visualize veins and quantify oxygen saturation. J Magn Reson Imaging. 2010; 32:663–676. [PubMed: 20815065]
13. Xu Y, Haacke EM. The role of voxel aspect ratio in determining apparent vascular phase behavior in susceptibility weighted imaging. Magn Reson Imaging. 2006; 24:155–160. [PubMed: 16455403]
14. Langham MC, Magland JF, Floyd TF, Wehrli FW. Retrospective correction for induced magnetic field inhomogeneity in measurements of large-vessel hemoglobin oxygen saturation by MR susceptometry. Magn Reson Med. 2009; 61:626–633. [PubMed: 19107914]
15. Jaramillo D, Villegas-Medina OL, Doty DK, Rivas R, Strife K, Dwek JR, Mulkern RV, Shapiro F. Age-related vascular changes in the epiphysis, physis, and metaphysis: normal findings on gadolinium-enhanced MRI of piglets. AJR Am J Roentgenol. 2004; 182:353–360. [PubMed: 14736661]
16. Ytrehus B, Carlson CS, Ekman S. Etiology and pathogenesis of osteochondrosis. Vet Pathol. 2007; 44:429–448. [PubMed: 17606505]
17. Carlson CS, Meuten DJ, Richardson DC. Ischemic necrosis of cartilage in spontaneous and experimental lesions of osteochondrosis. J Orthop Res. 1991; 9:317–329. [PubMed: 2010836]
18. Babyn PS, Kim HK, Lemaire C, Gahunia HK, Cross A, DeNanassy J, Pritzker KP. High-resolution magnetic resonance imaging of normal porcine cartilaginous epiphyseal maturation. J Magn Reson Imaging. 1996; 6:172–179. [PubMed: 8851424]
19. Jaramillo D, Villegas-Medina OL, Doty DK, Dwek JR, Ransil BJ, Mulkern RV, Shapiro F. Gadolinium-enhanced MR imaging demonstrates abduction-caused hip ischemia and its reversal in piglets. AJR Am J Roentgenol. 1996; 166:879–887. [PubMed: 8610567]
20. Barnewolt CE, Shapiro F, Jaramillo D. Normal gadolinium-enhanced MR images of the developing appendicular skeleton: Part I. Cartilaginous epiphysis and physis. AJR Am J Roentgenol. 1997; 169:183–189. [PubMed: 9207522]
21. Laor T, Jaramillo D. MR imaging insights into skeletal maturation: what is normal? Radiology. 2009; 250:28–38. [PubMed: 19092089]
22. Chung SM. The arterial supply of the developing proximal end of the human femur. J Bone Joint Surg Am. 1976; 58:961–970. [PubMed: 977628]
23. Metzger GJ, Auerbach EJ, Akgun C, Simonson J, Bi X, Ugurbil K, van de Moortele PF. Dynamically applied B(1) (+) shimming solutions for non-contrast enhanced renal angiography at 7.0 tesla. Magn Reson Med. 2013; 69:114–126. [PubMed: 22442056]

24. Van de Moortele PF, Akgun C, Adriany G, Moeller S, Ritter J, Collins CM, Smith MB, Vaughan JT, Ugurbil K. B(1) destructive interferences and spatial phase patterns at 7 T with a head transceiver array coil. Magn Reson Med. 2005; 54:1503–1518. [PubMed: 16270333]
25. Ellermann J, Goerke U, Morgan P, Ugurbil K, Tian J, Schmitter S, Vaughan T, Van De Moortele PF. Simultaneous bilateral hip joint imaging at 7 Tesla using fast transmit B(1) shimming methods and multichannel transmission - a feasibility study. NMR Biomed. 2012; 25:1202–1208. [PubMed: 22311346]
26. Van de Moortele, P-F.; Ugurbil, K. Very fast multi channel B1 calibration at high field in the small flip angle regime. Proceedings of the 17th Annual Meeting of ISMRM; Honolulu, Hawaii, USA. 2009. p. 367
27. Wang Y, Yu Y, Li D, Bae KT, Brown JJ, Lin W, Haacke EM. Artery and vein separation using susceptibility-dependent phase in contrast-enhanced MRA. J Magn Reson Imaging. 2000; 12:661–670. [PubMed: 11050635]
28. Reichenbach JR, Barth M, Haacke EM, Klarhofer M, Kaiser WA, Moser E. High-resolution MR venography at 3.0 Tesla. J Comput Assist Tomogr. 2000; 24:949–957. [PubMed: 11105717]
29. Rosset A, Spadola L, Ratib O. OsiriX: an open-source software for navigating in multidimensional DICOM images. J Digit Imaging. 2004; 17:205–216. [PubMed: 15534753]
30. Khanna PC, Thapa MM. The growing skeleton: MR imaging appearances of developing cartilage. Magn Reson Imaging Clin N Am. 2009; 17:411–421. v. [PubMed: 19524193]
31. Dixon JE, Simpson A, Mistry N, Evangelou N, Morris PG. Optimisation of T(2)(*)-weighted MRI for the detection of small veins in multiple sclerosis at 3 T and 7 T. Eur J Radiol. 2013; 82:719–727. [PubMed: 22138119]

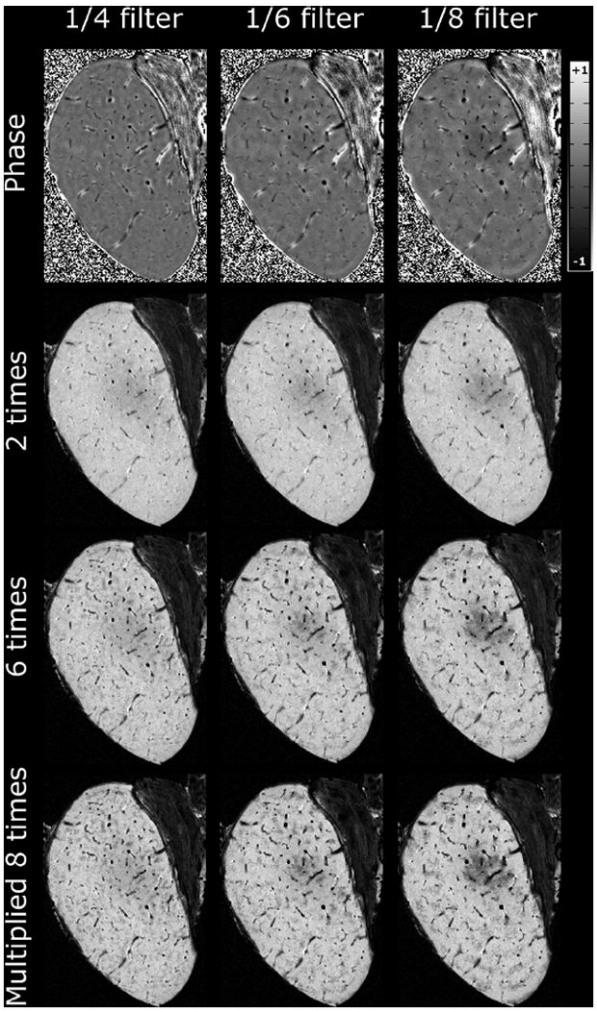

FIG. 1.

High-pass filtering and phase mask multiplication, axial slice through medial femoral condyle of a 3-week-old piglet, data from 9.4 T. First row: homodyne-filtered phase data with different sizes of k-space center used for the process. The other rows demonstrate the appearance of the processed data after different number of multiplications of the phase mask to the magnitude data for each different high-pass filtering.

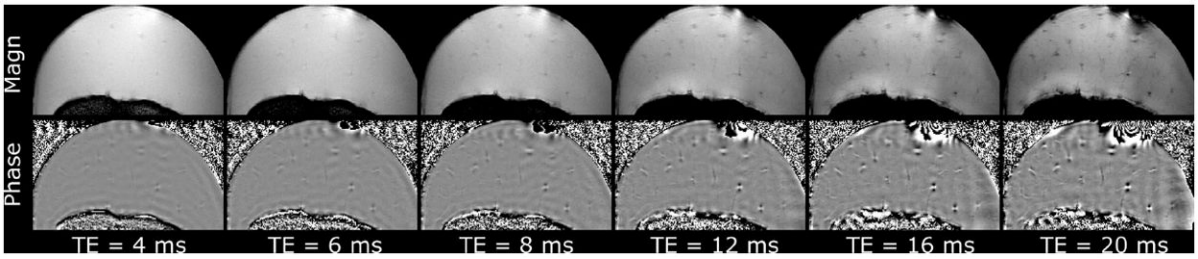

FIG. 2.

Effect of the TE on magnitude and filtered phase images at 9.4 T in a femoral condyle of an 8-week-old piglet. Effect of increasing TE was investigated using 2D-GRE sequence and post-processing as described in the methods. The vessels were already visualized at fairly short TEs, with increasing contrast between the vessels and surrounding matrix at increasing TEs.

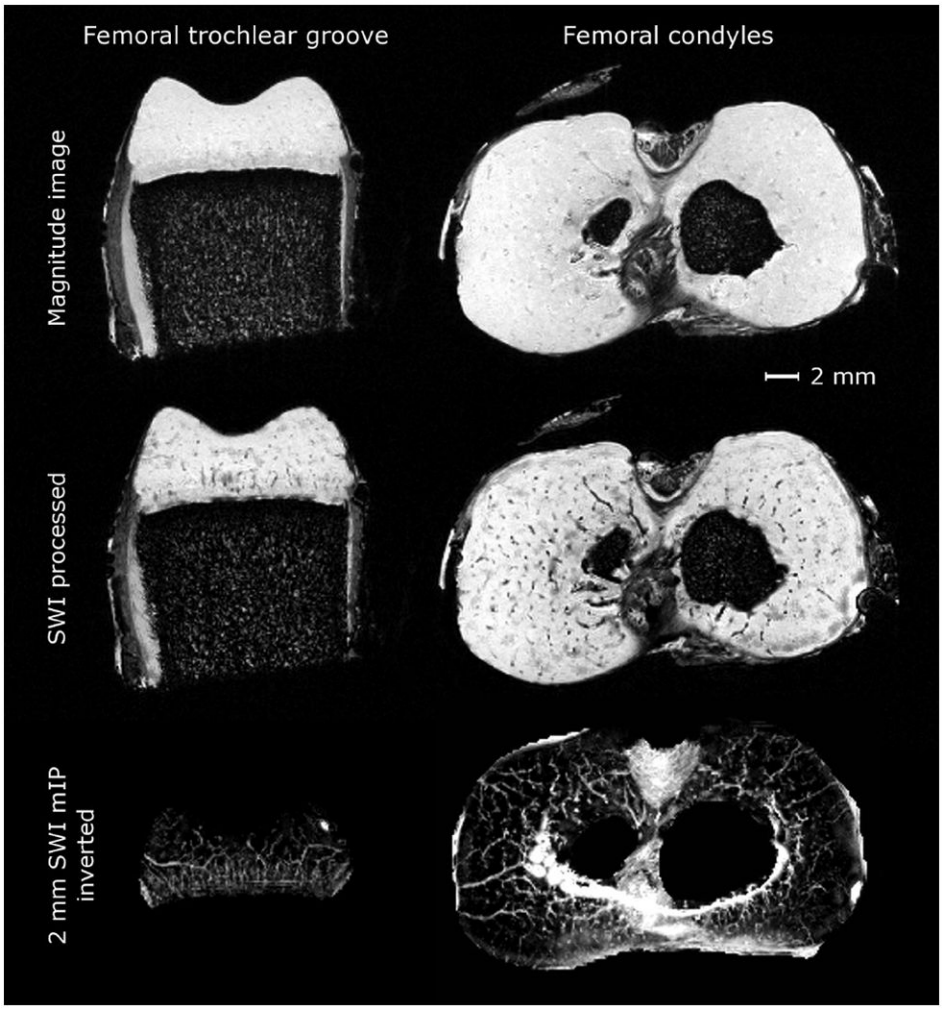

FIG. 3.

Raw GRE data and effect of SWI processing, data from 9.4 T. First row: raw GRE data in axial slices through distal femoral trochlea and condyles in a specimen from 1-week-old piglet. Second row: marked increase in the visibility of the vessels over the raw GRE data after SWI post-processing. Third row: further improvement in the visualization was achieved by generating a mIP over selected thickness (2 mm). The background was removed from the inverted data using thresholding.

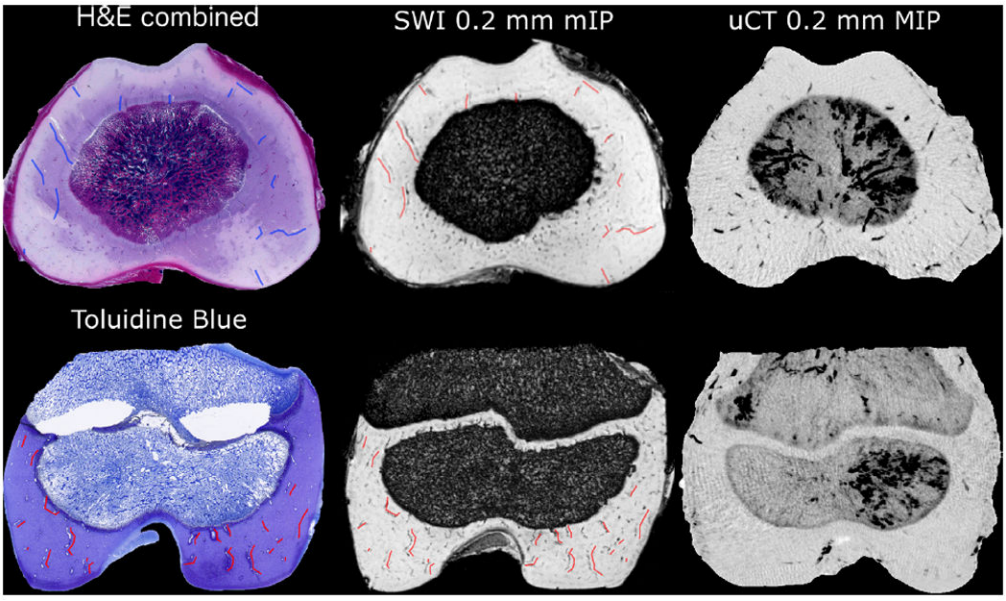

FIG. 4.

Hematoxylin & Eosin–stained histological sections (average of 5 sections 50 μm apart covering 200 μm thickness) demonstrating the cartilage canals in axial section of the distal femur of a 1-week-old piglet (top row) and Toluidine blue-stained histological section demonstrating cartilage canals in coronal section of the distal femur of a 3-week-old piglet (bottom row). SWI-processed data (9.4 T), sliced in a plane equal to the histology section and mIPped over 200 μm and μCT maximum intensity projection over the same thickness in the contralateral barium-perfused distal femur. Colored markings overlaid on histology (blue/red) and matching imaging slice from SWI data (red) point out some of the canals identified by both methods, demonstrating the agreement.

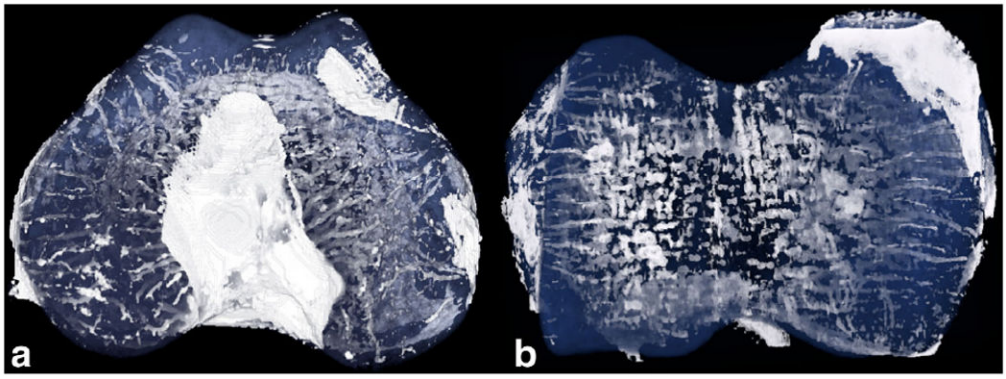

FIG. 5.

Projection of a 3D-volume rendering of the SWI dataset of (**a**) distal femur and (**b**) distal humerus of a 1-week-old piglet, data from 9.4 T. Background and bone were removed before the visualization using appropriate thresholding and masking. A color lookup table was created with opaque white for signal intensity corresponding to vessels and semitransparent blue for the epiphyseal cartilage matrix. Signal intensity similar to the vessels for ligaments, most notably in the intercondylar notch, was seen.

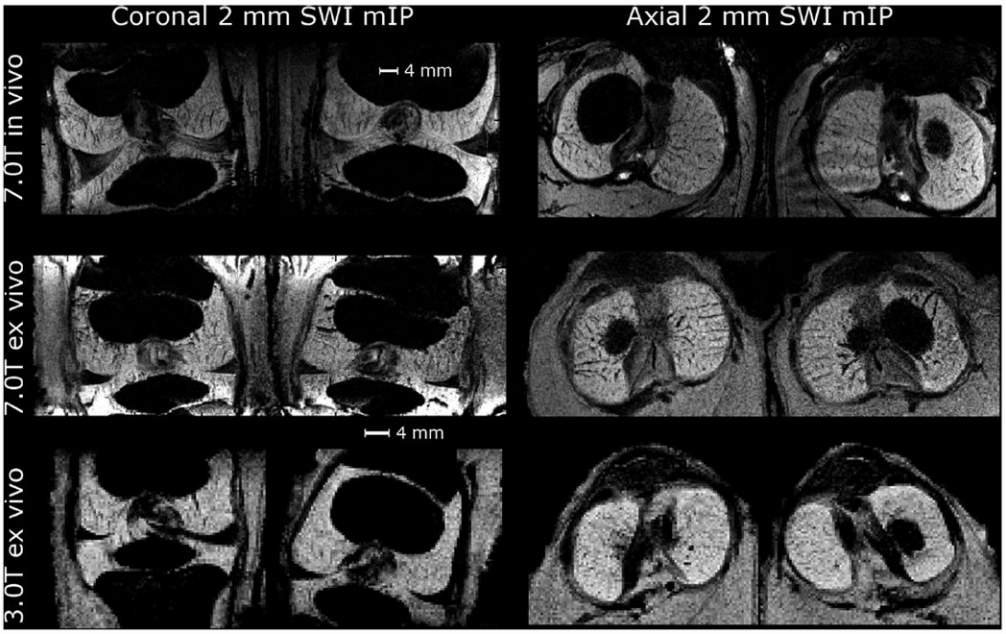

FIG. 6.

Coronal and axial mIPs of the SWI data over 2 mm thickness for 3-week-old piglet in vivo at 7.0 T and for carcass of a 2-week-old piglet ex vivo at 7.0 and 3.0 T. In all cases shown, vendor-provided post-processing was used.

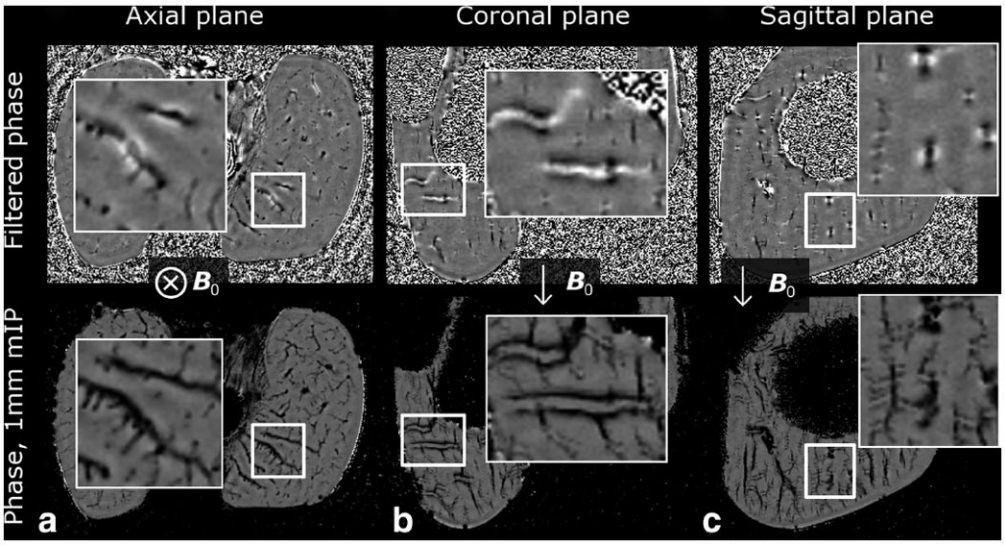

FIG. 7.

Demonstration of the dipolar phase pattern in high-resolution phase images at 9.4 T (data from 3-week-old piglet). The first row shows a single slice from the filtered phase data and the second row shows a 1 mm thick minimum intensity projection (mIP) of the phase to emphasize the differences in the appearance of the phase in different planes. **a**: axial plane, perpendicular to the B0 field showed a pattern of negative phase in the vessels surrounded by a faint halo of positive phase. **b, c**: Planes parallel to the B0 showed the dipolar appearance of the phase: positive phase through the vessel with negative spot above and below were noted. For vessels running perpendicular to the B0, artifactual “doubling” was noted in coronal and sagittal planes [particularly visualized in the zoomed mIPped view of (b)]. In axial plane, especially with mIP, no doubling artifact could be detected.

Table 1

Scanning Parameters and Post-Processing Setup for the Different Field Strengths and Experiments

B_0	9.4 T	7.0 T	7.0 T	3.0 T
Scan	Ex Vivo	In Vivo	Ex Vivo	Ex Vivo
TR/TE (ms)	40/14	27/15	26/13	45/28
BW (Hz/pixel)	~43	90	80	40
Flip angle (deg)	15	15	15	15
Resolution (μm)	~100	250	210	375
Matrix, slices	256^3–384^3	384 × 384, 144	384 × 384, 120	320 × 240, 88
Averages	1	3	2	1
Accelerations	–	GRAPPA = 2, Partial Fourier = 6/8[a]	GRAPPA = 2, Partial Fourier = 6/8[a]	–
Flow compensation	–	Yes	Yes	Yes
Scan time (min)	43–98	22:41	11:07	15:54
Post-processing	In-house, according to Haacke (4)	Vendor-provided and in-house	Vendor-provided	Vendor-provided

[a] Both slice and phase partial Fourier.